Nanoscale Advances

ROYAL SOCIETY OF CHEMISTRY

PAPER

View Article Online
View Journal | View Issue

Check for updates

Cite this: *Nanoscale Adv.*, 2021, **3**, 6992

Water dissociation and association on mirror twin boundaries in two-dimensional $MoSe_2$: insights from density functional theory calculations†

T. Joseph,[a] M. Ghorbani-Asl,[b] M. Batzill[c] and Arkady V. Krasheninnikov*[a]

Received 8th June 2021
Accepted 21st October 2021

DOI: 10.1039/d1na00429h

rsc.li/nanoscale-advances

The adsorption and dissociation of water molecules on two-dimensional transition metal dichalcogenides (TMDs) is expected to be dominated by point defects, such as vacancies, and edges. At the same time, the role of grain boundaries, and particularly, mirror twinboundaries (MTBs), whose concentration in TMDs can be quite high, is not fully understood. Using density functional theory calculations, we investigate the interaction of water, hydroxyl groups, as well as oxygen and hydrogen molecules with $MoSe_2$ monolayers when MTBs of various types are present. We show that the adsorption of all species on MTBs is energetically favorable as compared to that on the basal plane of pristine $MoSe_2$, but the interaction with Se vacancies is stronger. We further assess the energetics of various surface chemical reactions involving oxygen and hydrogen atoms. Our results indicate that water dissociation on the basal plane should be dominated by vacancies even when MTBs are present, but they facilitate water clustering through hydroxyl groups at MTBs, which can anchor water molecules and give rise to the decoration of MTBs with water clusters. Also, the presence of MTBs affects oxygen reduction reaction (ORR) on the $MoSe_2$ monolayer. Unlike Se vacancies which inhibit ORR due to a high overpotential, it is found that the ORR process on MTBs is more efficient, indicating their important role in the catalytic activity of $MoSe_2$ monolayer and likely other TMDs.

1 Introduction

Due to their diverse electronic,[1–4] optical,[4–7] magnetic,[8,9] and catalytic properties,[3,10–12] transition metal dichalcogenides (TMDs) are currently among the most intensively studied two-dimensional (2D) materials. The diversity in their properties stems not only from various possible chemical compositions of TMDs,[13] but also from the possibility to exist in different phases[13,14] and strong dependence of the electronic structure on the number of layers.[1] Moreover, the 2D nature of these systems enables modification of their properties by defects which can easily be introduced during or after the growth by chemical treatment or irradiation, see ref. 15 and 16 for an overview.

Not only point, but also line defects have been reported to exist in TMDs.[17–21] Among them, mirror twin boundaries (MTBs) of various types[22] with relatively low formation energies have been found. Moreover, contrary to serpentine or low-angle grain boundaries,[17,18] which appear during the growth when domains with arbitrary crystal orientation coalesce, the formation of straight MTBs is energetically favorable in non-stoichiometric chalcogen-deficient TMDs.[23] Indeed, their appearance in originally pristine TMD samples has been observed under electron irradiation, which created chalcogen vacancies[23–25] or Mo deposition[26] at moderate temperatures. Most important, their concentration can be very high,[20] and to some extent, controlled using the post-synthesis approaches described above.

TMDs, which are considered as an alternative to expensive Pt-based materials,[27,28] have received a considerable amount of attention in the context of catalysis,[3,10–12,29] *e.g.*, for the oxygen reduction reaction (ORR), which is one of the most important processes in proton exchange membrane fuel cells. Edges of TMDs have been shown to be catalytically active[29–33] but unless flakes of small sizes are used,[34] their concentration is naturally relatively low. Thus possible activation of the inert basal planes of TMDs has been studied. In particular, substitutional doping with P, N, O, Cu was proposed to be a method for activating the basal plane for ORR *via* enhancement of oxygen molecule adsorption.[35–37] However, this approach still requires the incorporation of impurities into the 2D materials during the growth or *via* a post-growth treatment. In addition, point defects like vacancies can create active sites for ORR electrocatalytic activity as shown for WTe_2.[38] Due to their metallic properties,[22,39–41] MTBs can potentially be active sites for the

---

[a] *Institute of Ion Beam Physics and Materials Research, Helmholtz-Zentrum Dresden-Rossendorf, 01328 Dresden, Germany. E-mail: t.joseph@hzdr.de; a.krasheninnikov@hzdr.de*

[b] *Department of Physics, University of South Florida, Tampa, FL 33620, USA*

[c] *Department of Applied Physics, Aalto University, P.O. Box 11100, 00076 Aalto, Finland*

† Electronic supplementary information (ESI) available. See DOI: 10.1039/d1na00429h

ORR process. However, the catalytic performance of ORR on these defects, which is critical for catalysis, has not been investigated so far. Moreover, the dissociation/association of water molecules and the behavior of their derivatives (hydroxyl groups and isolated O/H atoms) on TMDs with MTBs has not been addressed, contrary to that on basal planes and edges,[42–44] while knowing the energetics of these processes is important not only for assessing the catalytic properties but also for understanding the stability of TMDs at ambient conditions and clustering of water molecules at the surface.[45]

Here, using first-principles calculations, we theoretically study the interaction of water, hydroxyl groups, as well as hydrogen and oxygen atoms with MTBs of various types in $MoSe_2$ monolayer, a typical TMD. As a reference, we also study the interaction of these species with vacancies and pristine basal plane. The efficiency of ORR on the MTBs is investigated as well.

2 Methods

Spin-polarized density functional theory (DFT) calculations were performed using the generalized gradient approximation (GGA) with PBE exchange-correlation functional,[46] as implemented in the VASP code.[47,48] A plane-wave cut-off of 450 eV was used in all the calculations. A vacuum space of around 20 Å was considered in the confinement directions to avoid the spurious inter-layer interaction. The full geometry optimizations were carried out with the force tolerance being set to 0.01 eV Å^{-1}. The Brillouin zone of the supercells was sampled using gamma point approximation. The calculations include a dispersion correction scheme (DFT-D2)[49] for the effects of long-range vdW interactions. Calculations with a more accurate vdW exchange-correlation functional based on the Tkatchenko and Scheffler (DFT-TS) method[50] were also carried out for test systems. The structural models include nanoribbons of $MoSe_2$ with maximum number of 590 atoms, corresponding to 5 × 20 unit cells of an ideal lattice in a rectangular representation. The adsorption energy (E_{ads}) of the adsorbate on the surface is defined as:

$$E_{\text{ads}} = E_{\text{slab+adsorbate}} - (E_{\text{slab}} + E_{\text{adsorbate}}) \quad (1)$$

where the first term denotes the total energy of the slab with adsorbate, and the second and third terms represent the energy of the isolated slab and the isolated adsorbate, respectively.

The ORR reaction involves the trapping of adsorbate on a surface immersed in an electrolyte solution followed by a series of intermediate reactions,[51,52] eventually resulting in the reduction of O_2 to H_2O. Here, we employ the computational hydrogen electrode model (CHE) proposed in ref. 53 to describe the Gibbs free energy difference ΔG of each ORR elementary steps. ΔG is expressed as:

$$\Delta G = \Delta E + \varDelta_{\text{ZPE}} - T\Delta S + \Delta G_{\text{U}} + \Delta G_{\text{pH}} \quad (2)$$

where ΔE represents the change in the internal energy, $\varDelta_{\text{ZPE}}$ is the change in the vibrational zero-point energy, T is the temperature (298.15 K), ΔS is the entropy difference, ΔG_{U} and ΔG_{pH} are the contribution from electrode potential and pH of the solution. The reaction energy, ZPE and entropy change of the intermediate adorbate stages can be directly calculated from the corresponding DFT and vibrational calculations. The entropy is derived by calculating the vibrational entropy using harmonic approximation on the vibrational frequencies as input. However, the ZPE energies and entropies of liquid H_2O and gaseous H_2 are more complex, including the contributions from vibrations, rotations, and translations of molecules; fortunately these can be obtained from the thermodynamic NIST-JANAF tables.[54] The last two energy terms in eqn (2), for solution acidity ($\Delta G_{\text{pH}} = k_{\text{B}}T \ln 10 \times \text{pH}$) and electrode potential ($\Delta G_{\text{U}} = -qU$, $q = e|$ here) needs to be considered only for the protonation steps.

The ORR process in acidic involves a $4e^-$ associate or a $2e^-$ dissociative mechanism to reduce oxygen molecule to water. The major reaction pathway for $4e^-$ process employs:[53]

$$^*O_2 + H^+ + e^- \leftrightarrow {}^*OOH \quad (3)$$

$$^*OOH + H^+ + e^- \leftrightarrow {}^*O + H_2O \quad (4)$$

$$^*O + H^+ + e^- \leftrightarrow {}^*OH \quad (5)$$

$$^*OH + H^+ + e^- \leftrightarrow H_2O \quad (6)$$

where * implies the substrate with the respective adsorbate. In principle, the adsorption of molecular O_2 on the surface should also be included, but this is viewed as a chemical step and the steady-state adsorption of such neutral species does not contribute to the potential dependence of the faradaic current. The $2e^-$ dissociative mechanism involves adsorption of oxygen onto the substrate followed by step 5 and step 6. The presence of a finite electrode potential in the calculation of FED is due to the spontaneous charging of the surface during the ORR process. Thus, in this study we use $U = 1.23$ V at pH = 0 (acid solution). The detailed ORR equations are provided in the ESI.†

3 Result and discussion

3.1 Adsorption of water

To get a microscopic insight into the interaction of adsorbents on TMDs, the reactions on the pristine $MoSe_2$ sheets and those with MTBs were investigated. We considered three possible Mo-rich grain boundaries which are always lower in energy than Se-rich grain boundaries in the wide range of the chemical potential in TMDs.[23] In the 44| P and 44| E MTBs, the structure includes 4-fold rings that share a point at the Se site or edge (Mo–Se bond). The structure of the 55| 8 MTB contains two 5-fold rings adjacent to the 8-fold ring.

We first determined the atomic configurations of water adsorption on pristine $MoSe_2$. To identify the active sites for water adsorption, various initial molecule orientations on the top of the basal plane are investigated, see Fig. 1 and S1 in the ESI.† In the most stable configuration, the H_2O molecule is located ≈2.6 Å (the distance between the lower atom of the

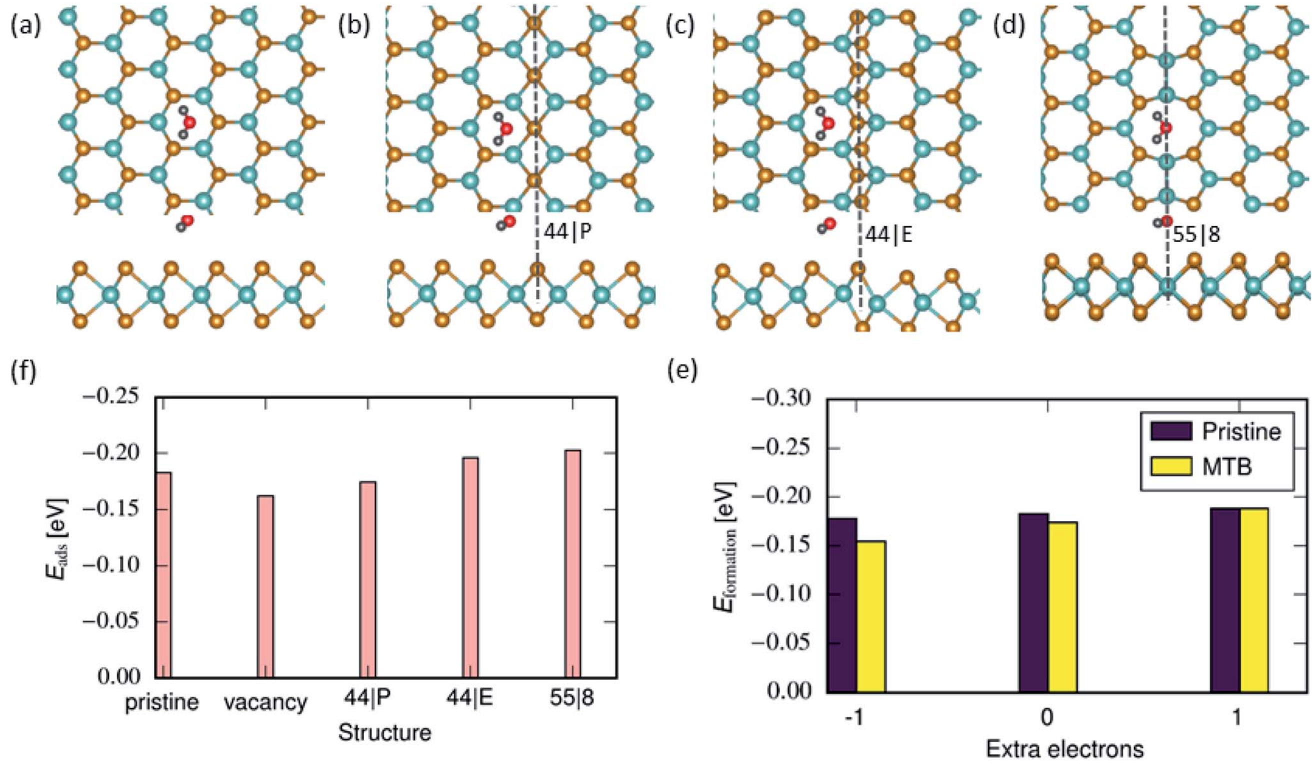

Fig. 1 Water adsorption on MoSe$_2$ monolayer: Atomic structures of 2D MoSe$_2$ with adsorbed water monomer on pristine (a), 44| P (b), 44| E (c) and 55| 8 (d) MTBs. (f) Adsorption energy of water monomers on top of MoSe$_2$ in the pristine area, vacancy and next to the MTB. (e) Adsorption energy of H$_2$O molecule on 44| P MTB when additional charge is present.

molecule and the uppermost Se atoms) above the center of the hexagon with the H atom pointing to the Se atoms of the monolayer. This is due to the electrostatic interaction between positively charged H atoms in water (+0.65 e) between and negatively charged Se plane, in agreement with the previous reports.[55]

The interaction of water with the basal plan of pristine MoSe$_2$ is mainly physisorption with an adsorption energy of ≈ -0.18 eV at the DFT-D2 level. Calculations using a more accurate DFT-TS method provided an adsorption energy of -0.15 eV. These values are consistent with the earlier theoretical reports[56] of water adsorption on MoS$_2$, indicating that perfect TMD monolayers have a hydrophobic character due to the chemically inert surface with saturated chalcogen ions. Similarly, in the case of a single Se vacancy, the small size of the defect does not permit the molecule to interact with positively charged Mo atoms causing a weak adsorption energy of ≈ -0.16 eV.

Contrary to edges or vacancies, the MTBs are devoid of undercoordinated atoms at the surface of the TMD monolayer. As a result, the adsorption energies for water molecules on top of MTBs differ only slightly (≈ 0.05 eV) in comparison to the pristine monolayer, as evident from Fig. 1. Fig. 1(b)–(d) illustrate the energetically favorable adsorption configurations of water molecule on various MTBs. It is found that the adsorption energy on the 55| 8 is the lowest followed by the 44| E and 44| P MTB. Unlike the adsorption configuration on the 44| E and 44| P MTBs, the plane of the molecule is almost parallel to the MoSe$_2$ basal plane and located on top of the 55| 8 MTB. The effect can be attributed to the presence of Mo–Mo bonds in the structure which are positively charged. Since MTBs have metallic states at the Fermi level[22,39–41] and additional charges can be localized in these structures, we also investigated the charging effects on the adsorption energy in 44| P MTB. It is found that extra electrons or holes (with a linear density of 0.05 e nm^{-1}) have minor effects on the adsorption energy on the 44| P MTB as evident from Fig. 1(e). The possible reason is that the Mo atomic layer is sandwiched between two Se atomic layers, and the extra charge mainly accumulated at Mo atoms is screened by Se atoms. It should be mentioned that in the case of additional positive charges, water molecules prefer adsorption in the pristine areas over that on 44| P MTBs.

3.2 Adsorption of hydroxyl groups

Fig. 2(a–d) show the lowest-energy configurations for hydroxyl groups adsorbed on the pristine basal plane, vacancy and various MTBs. The high chemical activity of OH as compared to that of H$_2$O originates from the difference in electronic structures of the molecules. The gap between the highest occupied (HOMO) and the lowest unoccupied molecular orbitals (LUMO) of hydroxyl is 1.53 eV which is significantly smaller than that of a water molecule (6.20 eV). Unlike water, HOMO and LUMO of hydroxyl are not center-symmetrical and are localized more on the oxygen than on the hydrogen atom. Accordingly, the interaction of hydroxyl with the basal plane of the monolayer is

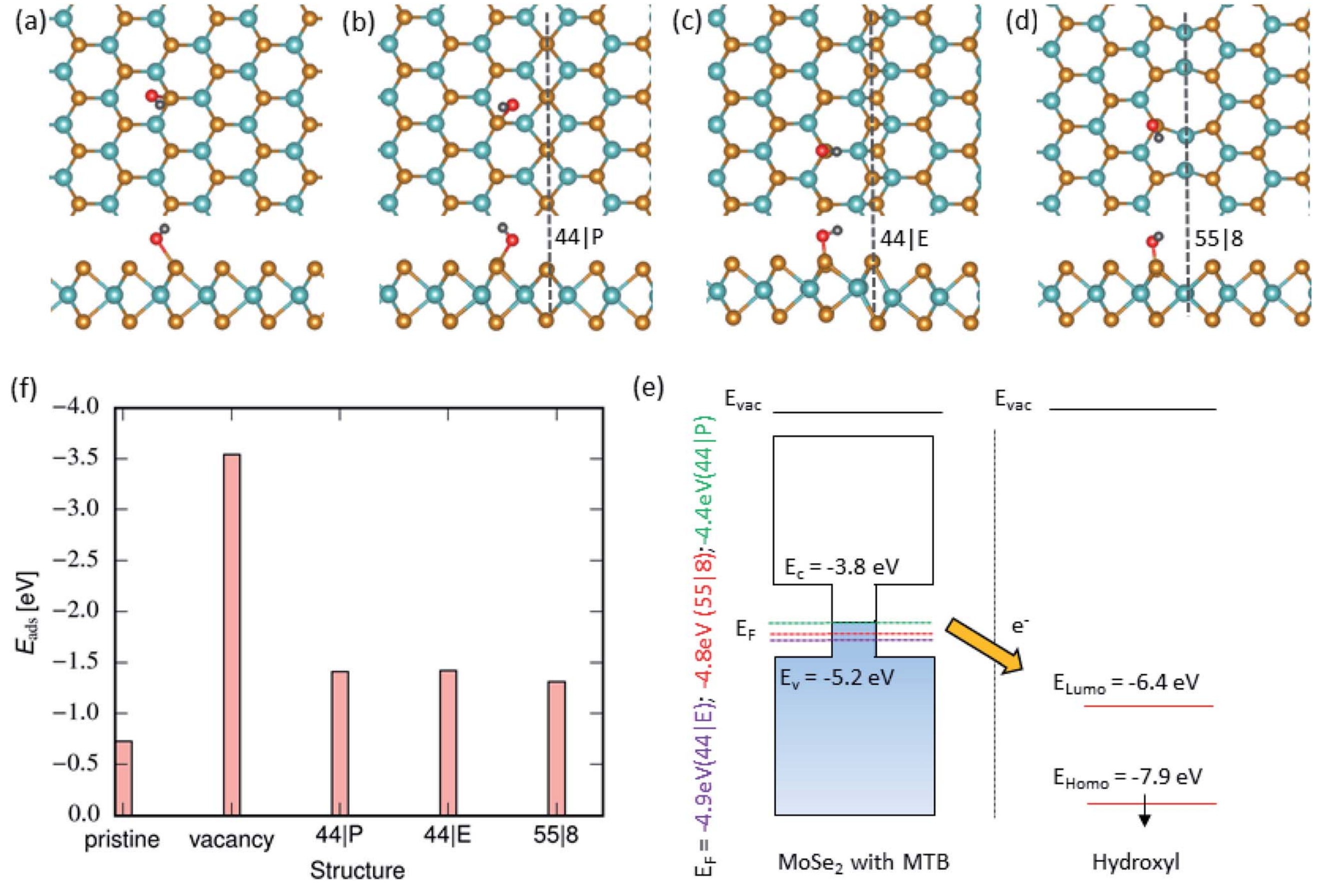

Fig. 2 Hydroxyl adsorption on $MoSe_2$ monolayer. (a)–(d) Atomic structures of 2D $MoSe_2$ with adsorbed hydroxyl radicals (top and side views). From left-to-right, the panels represent the lowest energy configurations of adsorbed hydroxyl groups in the pristine area and on the 44| P, 44| E and 55| 8 MTBs, respectively. (f) Adsorption energy of hydroxyl on top of $MoSe_2$ in the pristine area, vacancy and next to the MTBs. (e) Schematically representation of the electronic structure of $MoSe_2$ with various MTBs and isolated OH group.

stronger than for a water molecule. We found that the position of OH is energetically most preferable on top of the nearest-neighbor Se atoms next to the MTB. The adsorbed hydroxyl is oriented in such a way that the O atom is facing the Se atoms. Fig. 2(f) presents adsorption energies on different MTBs, which are very close to each other, with a difference of only ≈ 0.1 eV. The difference between adsorption energy at MTB to the pristine part is about 0.7 eV, as also illustrated in Fig. 2(f). This gives rise to a preferential adsorption of OH groups on MTBs. Moreover, the two spin-polarized LUMO states of the OH molecule are below the Fermi level, indicating a charge transfer from the $MoSe_2$ to the adsorbent, as seen in Fig. 2(f). In order to rationalize the strong molecule–MTB interaction, we also analyzed the electronic structure of the system after the adsorption of the molecule. Bader analysis was used to assess the charge transfer between molecules and the substrate. The hydroxyl group creates a strong bond by transferring charge from the MTB to the hydroxyl group. Since MTBs are metallic, the charge transfer is larger as compared to the pristine system. In the case of a single vacancy, the anchoring atom *i.e.* oxygen, occupy the vacancy forming a strong bond with Mo atoms. The adsorption energy at vacancy sites is lower than that on MTBs by ≈ 2 eV.

3.3 Adsorption of oxygen

Next, we explored the adsorption of an O atom on the $MoSe_2$ monolayer. It is known that point defects in TMDs, such as S-vacancies, can be active sites for dissociation of O_2 molecules.[57] Our calculations indicate that one needs 3.04 eV per atom for an isolated O_2 molecule to dissociate. Thus, in agreement with the results of earlier studies,[58] it is energetically unfavorable for the molecule to dissociate on pristine $MoSe_2$ monolayer, as evident from Fig. 3(f), but the dissociation is exothermic on a vacancy, assuming that one O atoms takes the substitutional position and forms strong covalent bonds with the three adjacent Mo atoms, and the other is adsorbed on the surface. After dissociation, the other O atoms can diffuse to the surrounding area on the sample surface. Therefore, it is imperative to explore the interaction of an adsorbed O atom with MTBs in the $MoSe_2$ monolayer. We found that the oxygen atom prefers to sit on top of the chalcogen atom as shown in Fig. 3(a–c). The only exception is the 55| 8 MTB, where oxygen atom is adsorbed in the middle of the Mo–Mo stripe, Fig. 3(d). The adsorption energy of the oxygen atom is naturally lower than that of the water molecule as the atom is chemisorbed on the surface. As compared to hydroxyl, the lower adsorption energies indicate stronger interaction of oxygen with $MoSe_2$. The strong interaction with the 55| 8 MTB can also be

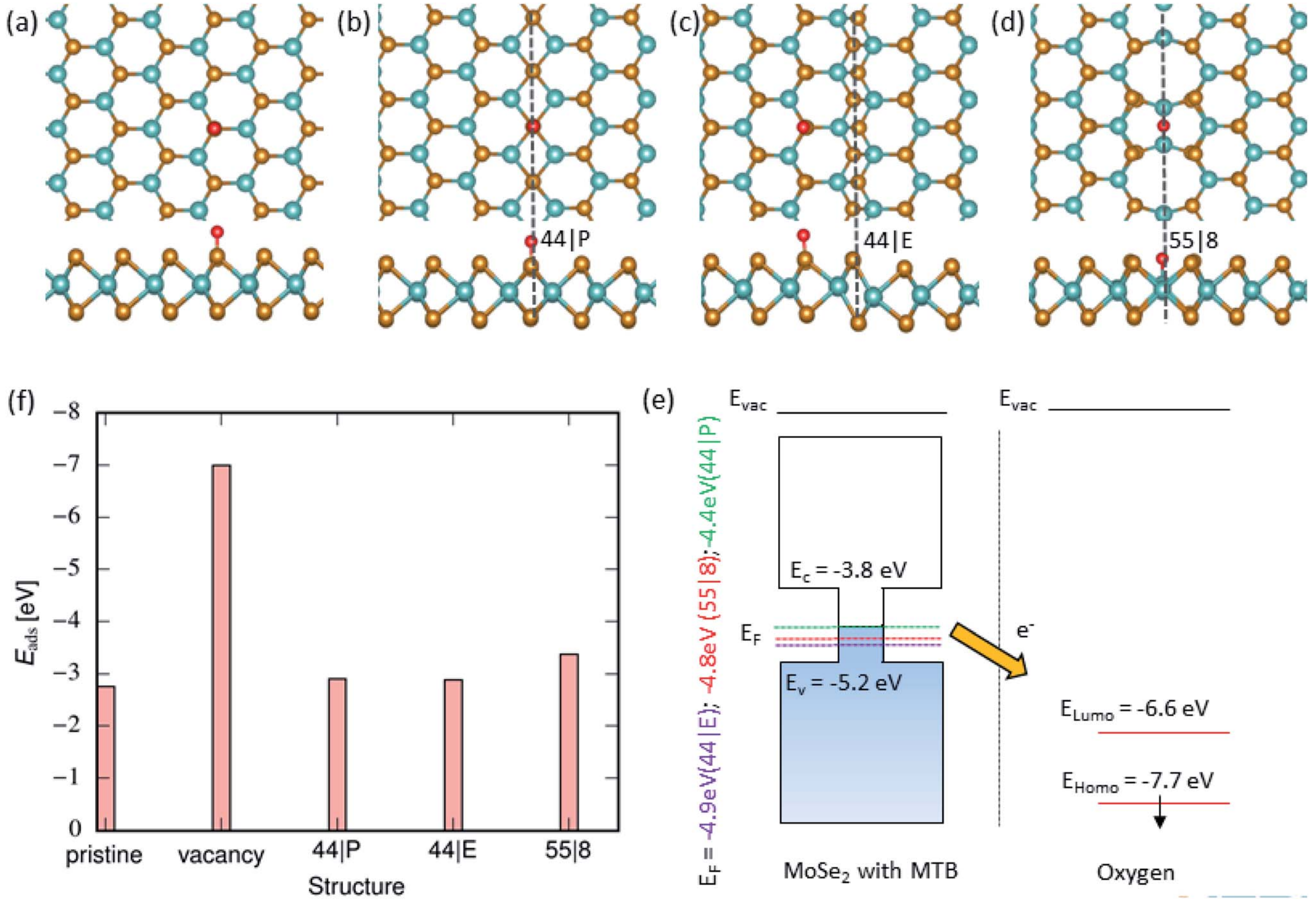

Fig. 3 Oxygen adsorption on MoSe$_2$ monolayer. (a)–(d) Atomic structures of 2D MoSe$_2$ with adsorbed oxygen (top and side views). From left to right, the panels shown the lowest energy configurations of adsorbed oxygen in the pristine area, on the 44| P, 44| E and 55| 8 MTBs, respectively. (f) Adsorption energy of oxygen on top of MoSe$_2$ in the pristine area, vacancy and next to the MTBs. (f) Schematically illustration of the electronic structure of MoSe$_2$ with MTB and isolated O atom.

deduced from the charge transfer picture given in Fig. 3. In addition, the adsorption of the O_2 molecule on the 55| 8 MTB was studied. The adsorption energy of −0.090 eV was found. From Fig. S3,† by comparing the adsorption energies of the O_2 molecule and two O atoms, it is clear that the adsorbed molecule may spontaneously dissociate to form two adsorbed O atoms and releasing energy of 0.86 eV.

Fig. 3(f) presents a comparison of adsorption energies at different MTBs. Among all the MTBs, the 55| 8 MTB shows the lowest adsorption energy, −3.4 eV, which corresponds to the strongest interaction between O and surface. Unlike OH adsorption, the difference in O adsorption energy between pristine and on the 44| P or 44| E MTBs is small ≈0.1 eV. The adsorption energy on the 55| 8 MTB is ≈0.6 eV lower than for the pristine sheet, suggesting preferential adsorption of O at the MTB. Besides, the adsorption of O is strongly influenced by presence of Se vacancies. The adsorption energy at vacancy sites is larger in comparison to MTB by ≈4 eV.

3.4 Adsorption of hydrogen

We further examined the energetics of adsorbed H atoms on the pristine MoSe$_2$ monolayer. The calculations indicate that H atoms in the interstitial configuration are energetically more favorable by 0.72 eV than adatom configurations. Using NEB method, we calculated the energy barrier along the path between adatom configuration in the hollow site and the corresponding interstitial position, as shown in Fig. 5. The data indicates that the transition between two configurations requires overcoming an energy barrier of *ca.* 0.45 eV. As compared to MoS$_2$, the larger primitive cell of MoSe$_2$ provide more free space for H in the interstitial position. Similar behavior has been reported for H[12] and transition metal atoms adsorbed on MoTe$_2$.[59] The lowest-energy position of H atoms in the Mo-atom plane indicates that H permeability of MoSe$_2$ should be quite different from that of MoS$_2$.

The strongest binding of an H atom to the 44| P and 44| E MTBs occurs at the center of the hexagon next to the MTB. For the 55| 8 MTB, however, H prefers to be embedded into the 8-fold ring of the MTB. Nevertheless, the adsorption energies of H atoms were found to be very similar for all types of MTBs. The selective adsorption of hydrogen can be attributed to the states available at the Fermi level. Similar to edge defects previously studied,[33,60] there are many sharp peaks near the Fermi level, indicating the existence of many free electrons that can readily

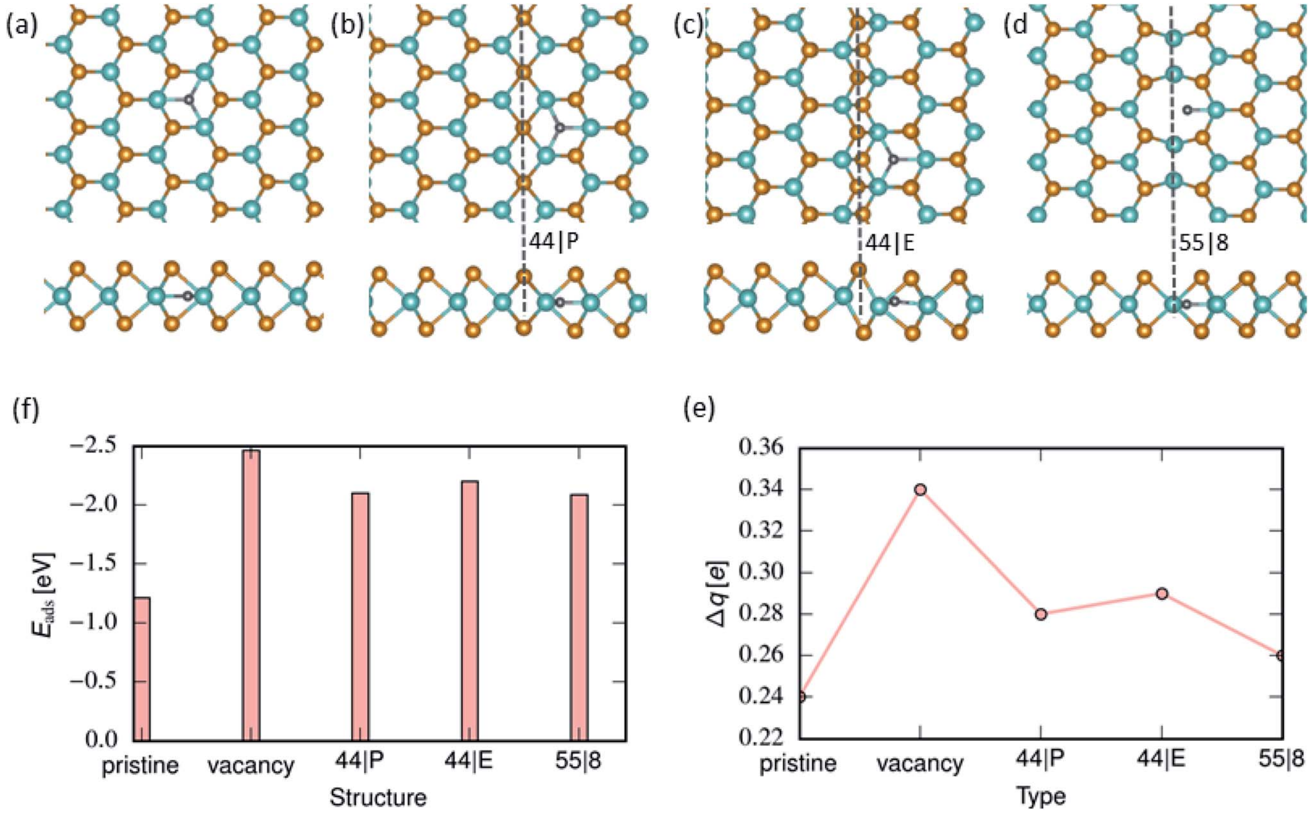

Fig. 4 Hydrogen adsorption on $MoSe_2$ monolayer. (a)–(d) Atomic structures of 2D $MoSe_2$ with an adsorbed hydrogen atom (top and side views). From left to right, the panels represent lowest energy configurations of adsorbed hydrogen atoms on pristine, 44| P, 44| E and 55| 8 MTBs respectively. (f) Adsorption energy of hydrogen atoms in the pristine area, on vacancy and next to MTBs. (e) Charge transferred from $MoSe_2$ to H group, as revealed by the Bader analysis.

redistribute under any chemical perturbation leading to selective adsorption. The calculated adsorption energies of H, Fig. 4(f) indicate that Se vacancy is the most favourable adsorption site, followed by MTBs. We further analyzed the charge transfer from substrate $MoSe_2$ to H atom. The results are presented in 4(e). H adsorption on Se vacancy site results in the largest charge transfer due to a strong interaction between the H atom and three adjacent Mo atoms. Moreover, the binding of hydrogen is stronger than that of the hydroxyl group, but weaker than the oxygen atom.

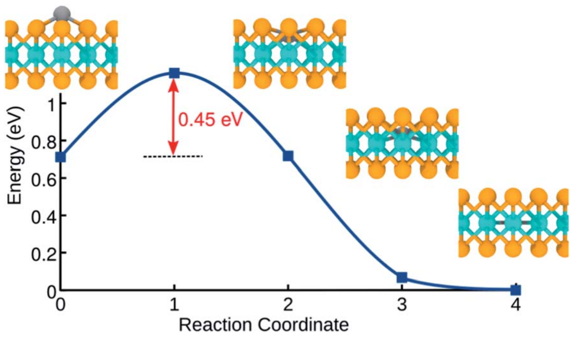

Fig. 5 Calculated energy profile of diffusion process for an adsorbed H atom on monolayer $MoSe_2$.

3.5 Water dissociation

Water dissociation is a key issue not only in the green production of hydrogen from water, but also because it plays an essential role in numerous catalytic reactions. The typical procedure for the hydrogen production from water on catalytic surfaces includes the splitting of water into adsorbed H and OH species ($H_2O + 2^* \leftrightarrow H^* + OH^*$). The adsorbed hydrogen atoms can join to form a molecule. Alternatively, the hydrogen atoms in the water molecule can be directly attached to form a hydrogen molecule thereby the separated O atom is adsorbed on the surface ($H_2O + {}^* \leftrightarrow O^* + H_2$). We evaluated the feasibility of these mechanisms that lead to the dissociation of a H_2O molecule at MTBs. Assuming that O_2 molecules adsorbed on vacancy sites can dissociate and the atoms diffuse on the outer Se plane, the important question is how these O atoms affect the dissociation of water on $MoSe_2$. Here we considered two possible scenarios, as shown in Fig. 6: the dissociation of water on (1) the pristine surface, and (2) the oxidized surface. First, the energy barrier for H_2O dissociation to OH radical and H on the pristine surface was evaluated. Our results show that an energy barrier of 2.97 eV is required to be overcome for the dissociation of water on the perfect basal plane, indicating that the direct dissociation is highly unlikely on a pristine $MoSe_2$ monolayer. In the case of MTBs, the dissociation barrier is

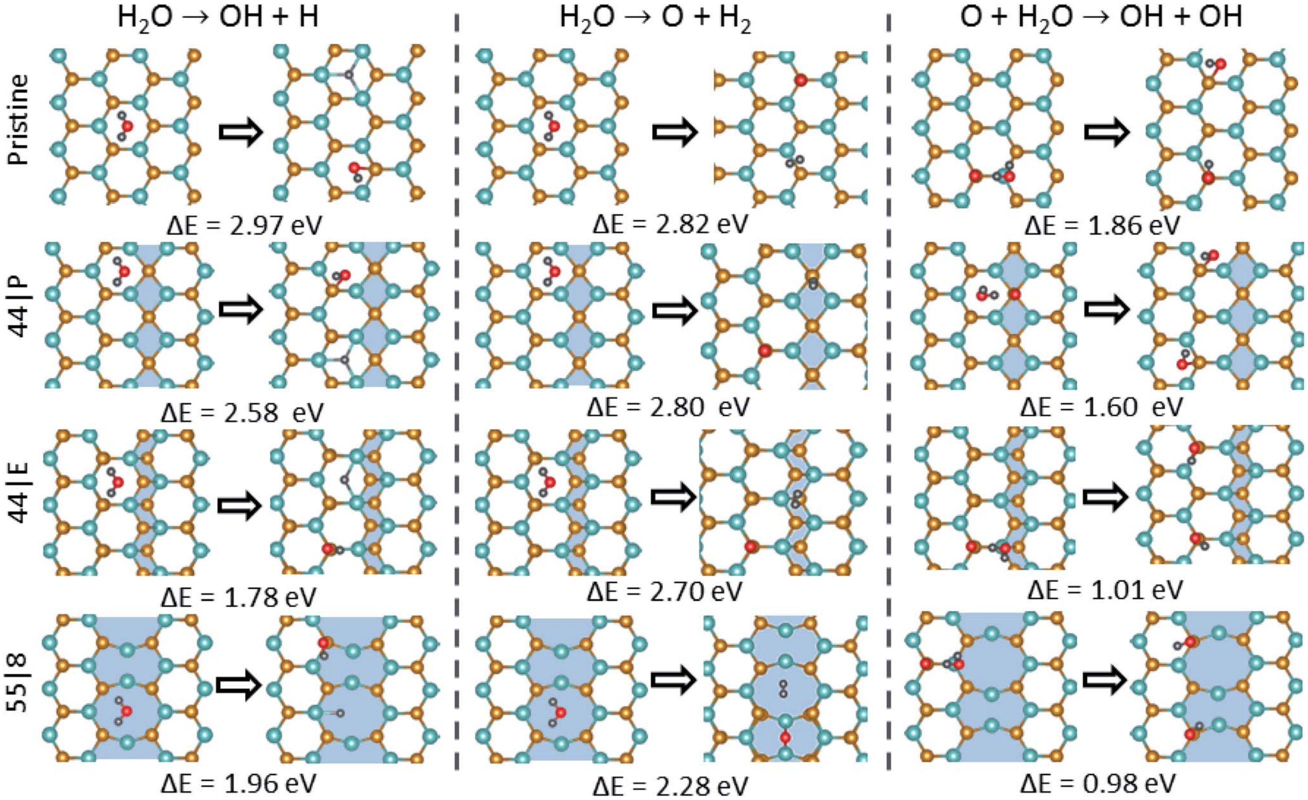

Fig. 6 Schematic view of water association and dissociation reactions and the energetics for the pristine system and that with 44| P, 44| E and 55| 8 MTBs.

reduced, where for instance the lowest barrier of 1.96 eV was found for the 55| 8 MTB. Similarly, the energy barrier for water dissociation to O atom and hydrogen molecule is lower for MTBs than the pristine sheet. We further investigated the effect of oxidation on the dissociation of the H_2O molecule. The presence of oxygen decreases the dissociation energy barrier by 1 eV as compared to the basal plane of the monolayer. In the case of MTBs, the energy barrier is further lowered by about 1 eV reaching to 0.98 eV for the 55| 8 MTB. Our findings suggest that the 55| 8 MTBs could be suitable defects for the dissociation of H_2O where a strong chemical reaction with OH is accomplished by the interchange of electrons with the adjacent Mo atoms resulting in the separation of H and O atoms.

3.6 Oxygen reduction reaction

The first step for ORR process involves the adsorption of oxygen molecules on the electrode. The corresponding structures and energies of the $MoSe_2$ sheets representing the electrodes are shown in Fig. 7. From calculation it is seen that oxygen molecules prefers to adsorb on vacancies in $MoSe_2$. The free-energy diagram for the associative ORR mechanism is shown in Fig. 8. The ORR performance for the pristine system and with MTBs is calculated at equilibrium potential of 1.23 V as mentioned in the method section. The overpotential is the minimum additional energy barrier required to be overcome for the ORR process,[53] meaning that the higher the overpotential, the more difficult the reaction becomes. With the 4e-process described in Fig. 8, the rate-determining step (RDS) is the protonation of the adsorbed oxygen to *OOH which requires the energy of 1.34 eV in the pristine case.This can be explained due to the weak vdW binding of O_2 molecule and the strong *OOH binding to the catalyst.[51,53] Hydrogen peroxide can be formed as an intermediate of ORR only by the $2e^-$ associative mechanism in eqn (4) instead of *O + H_2O. Hydrogen peroxide has been detected during ORR, but it remains unclear whether it is a key intermediate of the dominant ORR mechanism or a side-product.[61] The strong hydroperoxyl adsorption on $MoSe_2$ as shown in Fig. S2† favours O–O bond dissociation in the adsorbed *OOH. Thus all catalysts with strong interaction between the reaction site and O species could easily dissociate the O_2 molecule leading to H_2O formation, while a too-weak one leads to H_2O_2 reaction path.[53] Here, in this case due to the above mentioned property, a $4e^-$ oxygen reduction to water is preferred. Also, the kinetics for the H_2O_2 and H_2O pathways is shown in Fig. S4.† Although the determining step is the same as in the ORR process on MTBs, the overpotentials are reduced, following the order 44| P > 55| 8 > 44| E. Therefore, the ORR process on 44| E MTB is found to be more efficient, with the overpotential of 1.19 eV, in comparison to the pristine system and other investigated MTBs. Our results show that ORR in presence of Se vacancy follows a $2e^-$ process because of the absence of stable OOH adsorbates and strong adsorption of O_2 at the vacancy site (Fig. 8(b)).

The overpotential for pristine $MoSe_2$ is 1.34 V, significantly higher than 0.45 V of Pt electrocatalyst,[53] 0.47 V of defective

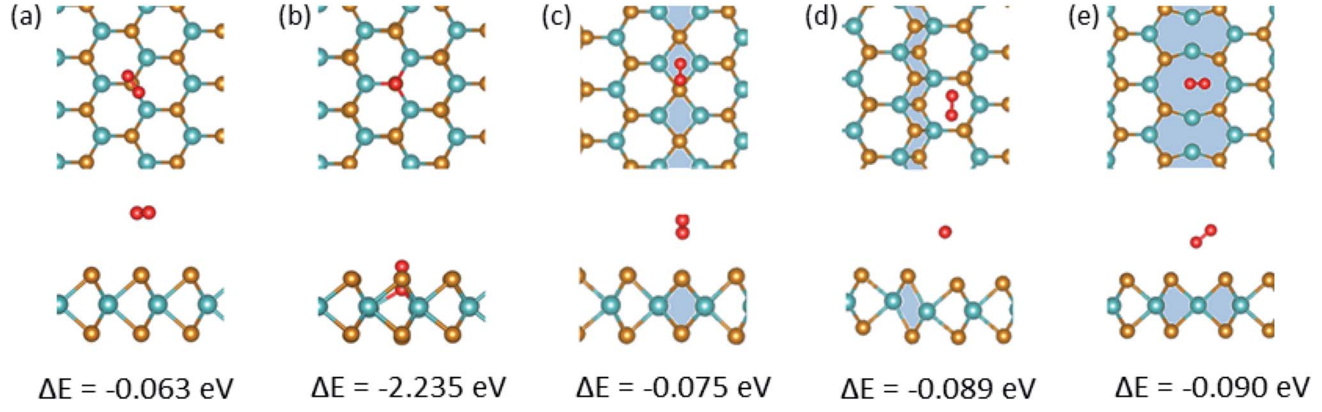

Fig. 7 Adsorption of O_2 molecules on $MoSe_2$ at various sites. (a) Pristine (b) Se vacancy (c) 44| P, (d) 44| E, (e) 55| 8 MTBs.

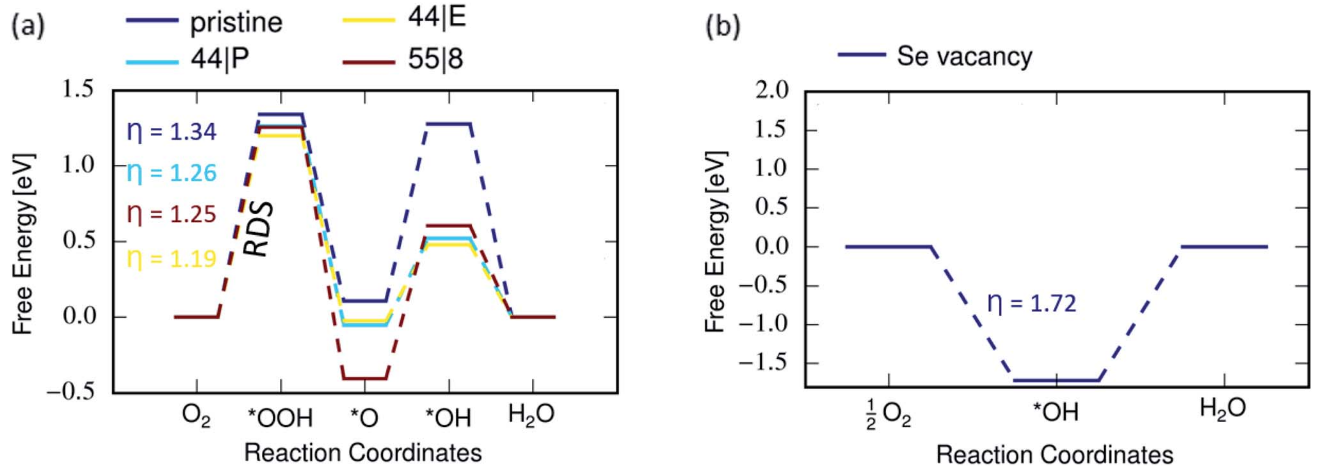

Fig. 8 Gibbs free energy diagrams of ORR along the (a) $4e^-$ pathway on pristine and defective $MoSe_2$; (b) $2e^-$ pathway for Se vacancy, where η denotes the overpotential.

graphene,[62] and 0.67 V of N-doped graphene.[63] The features of the Gibbs free energy diagram for $MoSe_2$ are similar to those reported for the defective WTe_2.[38] In the case of MTBs, the ORR overpotential is found to be ≈1.2 V indicating better ORR characteristics than at Se vacancy.

4 Conclusions

In conclusion, we investigated the adsorption of H_2O, OH, O, H and O_2 species on monolayer $MoSe_2$. The adsorption of H_2O is the weakest, with an adsorption energy ranging from −0.18 eV to −0.20 eV. On the other hand, adsorption of O is the strongest, with the adsorption energy being in the range of −2.8 eV to −3.4 eV. It is found that for all the considered adsorbates except for water, the most preferred site of adsorption are Se vacancies. We demonstrated that the adsorbed OH and O species can be used as anchor points for selective adsorption of water at MTBs (55| 8 MTB for O adsorption). We further investigated the water dissociation and association on different MTBs. From our calculation, it is evident that energy required for dissociation of water molecules is reduced by ≈1.0 eV as compared to the pristine area when it happens on a 55| 8 MTB. With regard to the behavior of O_2, calculations show that oxygen prefers to adsorb as dissociated atoms on the 55| 8 MTB rather than as a molecule. Moreover, ORR process on pristine $MoSe_2$ and MTBs has lower overpotential than on a Se vacancy, thus indicating better ORR efficiency than at vacancies. Although, based on the results of previous studies,[30,31] the ORR reactivity at edges is expected to be higher than at MTBs, potentially much higher concentration of MTBs, which can be produced during or after the growth by TM atom deposition[26] or electron beam irradiation,[23–25] in comparison to edges, suggests that MTBs can have a strong influence on the ORR efficiency of $MoSe_2$ sheets. Overall, our findings provide important insights into the adsorption of water and its derivatives on $MoSe_2$ monolayers with MTBs which should be accounted for when assessing the catalytic performance of this material in electrochemical energy applications.

Conflicts of interest

There are no conflicts to declare.

Acknowledgements

We acknowledge funding from the German Research Foundation (DFG), projects KR 4866/2-1 and KR 4866/6-1. M. B. further acknowledges support from the National Science Foundation under awards NSF-CHE 1801199 and 2140038. The computational support from the Technical University of Dresden computing cluster (TAURUS), from High Performance Computing Center (HLRS) in Stuttgart, Germany, and CSC Finland, is gratefully appreciated.

Notes and references

1 K. F. Mak, C. Lee, J. Hone, J. Shan and T. F. Heinz, *Phys. Rev. Lett.*, 2010, **105**, 136805–136809.

2 A. Kuc, N. Zibouche and T. Heine, *Phys. Rev. B: Condens. Matter Mater. Phys.*, 2011, **83**, 245213–245217.

3 D. J. Late, Y.-K. Huang, B. Liu, J. Acharya, S. N. Shirodkar, J. Luo, A. Yan, D. Charles, U. V. Waghmare, V. P. Dravid and C. N. R. Rao, *ACS Nano*, 2013, **7**, 4879–4891.

4 Q. H. Wang, K. Kalantar-Zadeh, A. Kis, J. N. Coleman and M. S. Strano, *Nat. Nanotechnol.*, 2012, **7**, 699–712.

5 M. Chhowalla, H. S. Shin, G. Eda, L.-J. Li, K. P. Loh and H. Zhang, *Nat. Chem.*, 2013, **5**, 263–275.

6 Z. Li, Y. Xiao, Y. Gong, Z. Wang, Y. Kang, S. Zu, P. M. Ajayan, P. Nordlander and Z. Fang, *ACS Nano*, 2015, **9**, 10158–10164.

7 Z. Yin, H. Li, H. Li, L. Jiang, Y. Shi, Y. Sun, G. Lu, Q. Zhang, X. Chen and H. Zhang, *ACS Nano*, 2011, **6**, 74–80.

8 A. Avsar, C.-y. Cheon, M. Pizzochero, M. Tripathi, A. Ciarrocchi, O. V. Yazyev and A. Kis, *Nat. Commun.*, 2020, **11**, 4806.

9 P. M. Coelho, H.-P. Komsa, K. Lasek, V. Kalappattil, J. Karthikeyan, M. Phan, A. V. Krasheninnikov and M. Batzill, *Adv. Electron. Mater.*, 2019, **5**, 1900044.

10 Y. Kang, Y. Gong, Z. Hu, Z. Li, Z. Qiu, X. Zhu, P. M. Ajayan and Z. Fang, *Nanoscale*, 2015, **7**, 4482–4488.

11 S. Helveg, J. V. Lauritsen, E. Lægsgaard, I. Stensgaard, J. K. Nørskov, B. S. Clausen, H. Topsøe and F. Besenbacher, *Phys. Rev. Lett.*, 2000, **84**, 951–954.

12 T. Kosmala, H. C. Diaz, H.-P. Komsa, Y. Ma, A. V. Krasheninnikov, M. Batzill and S. Agnoli, *Adv. Energy Mater.*, 2018, **8**, 1800031.

13 A. Kolobov and J. Tominaga, *Two-Dimensional Transition Metal Dichalcogenides*, Springer, 2016.

14 V. Sorkin, H. Pan, H. Shi, S. Y. Quek and Y. W. Zhang, *Crit. Rev. Solid State Mater. Sci.*, 2014, **39**, 319–367.

15 Z. Lin, B. R. Carvalho, E. Kahn, R. Lv, R. Rao, H. Terrones, M. A. Pimenta and M. Terrones, *2D Materials*, 2016, **3**, 022002.

16 A. V. Krasheninnikov, *Nanoscale Horiz.*, 2020, **5**, 1447–1452.

17 A. M. van der Zande, P. Y. Huang, D. A. Chenet, T. C. Berkelbach, Y. You, G.-H. Lee, T. F. Heinz, D. R. Reichman, D. A. Muller and J. C. Hone, *Nat. Mater.*, 2013, **12**, 554–561.

18 W. Zhou, X. Zou, S. Najmaei, Z. Liu, Y. Shi, J. Kong, J. Lou, P. M. Ajayan, B. I. Yakobson and J.-C. Idrobo, *Nano Lett.*, 2013, **13**, 2615–2622.

19 O. Yazyev and Y. P. Chen, *Nat. Nanotechnol.*, 2014, **9**, 755–767.

20 K. Lasek, J. Li, S. Kolekar, P. M. Coelho, L. Guo, M. Zhang, Z. Wang and M. Batzill, *Surf. Sci. Rep.*, 2021, 100523.

21 M. Chubarov, T. H. Choudhury, D. R. Hickey, S. Bachu, T. Zhang, A. Sebastian, A. Bansal, H. Zhu, N. Trainor, S. Das, M. Terrones, N. Alem and J. M. Redwing, *ACS Nano*, 2021, **15**, 2532–2541.

22 H.-P. Komsa and A. V. Krasheninnikov, *Adv. Electron. Mater.*, 2017, **3**, 1600468.

23 O. Lehtinen, H.-P. Komsa, A. Pulkin, M. B. Whitwick, M.-W. Chen, T. Lehnert, M. J. Mohn, O. V. Yazyev, A. Kis, U. Kaiser and A. V. Krasheninnikov, *ACS Nano*, 2015, **9**, 3274–3283.

24 J. Lin, S. T. Pantelides and W. Zhou, *ACS Nano*, 2015, **9**, 5189–5197.

25 Y.-C. Lin, T. Björkman, H.-P. Komsa, P.-Y. Teng, C.-H. Yeh, F.-S. Huang, K.-H. Lin, J. Jadczak, Y.-S. Huang, P.-W. Chiu, A. V. Krasheninnikov and K. Suenaga, *Nat. Commun.*, 2015, **6**, 6736.

26 P. M. Coelho, H.-P. Komsa, H. Coy Diaz, Y. Ma, A. V. Krasheninnikov and M. Batzill, *ACS Nano*, 2018, **12**, 3975–3984.

27 U. Paulus, A. Wokaun, G. Scherer, T. Schmidt, V. Stamenkovic, N. Markovic and P. Ross, *Electrochim. Acta*, 2002, **47**, 3787–3798.

28 H. R. Colón-Mercado and B. N. Popov, *J. Power Sources*, 2006, **155**, 253–263.

29 X. Tong, X. Zhan, D. Rawach, Z. Chen, G. Zhang and S. Sun, *Prog. Nat. Sci.: Mater. Int.*, 2020, **30**, 787–795.

30 Y. Hao, L.-C. Xu, J. Pu, L. Wang and L.-F. Huang, *Electrochim. Acta*, 2020, **338**, 135865.

31 A. Y. S. Eng, A. Ambrosi, Z. Sofer, P. Šimek and M. Pumera, *ACS Nano*, 2014, **8**, 12185–12198.

32 W. Shi, K. Fan and Z. Wang, *Phys. Chem. Chem. Phys.*, 2018, **20**, 29423–29429.

33 C. Tsai, K. Chan, F. Abild-Pedersen and J. K. Nørskov, *Phys. Chem. Chem. Phys.*, 2014, **16**, 13156–13164.

34 B. Mohanty, M. Ghorbani-Asl, S. Kretschmer, A. Ghosh, P. Guha, S. K. Panda, B. Jena, A. V. Krasheninnikov and B. K. Jena, *ACS Catal.*, 2018, **8**, 1683–1689.

35 H. Huang, X. Feng, C. Du and W. Song, *Chem. Commun.*, 2015, **51**, 7903–7906.

36 H. Huang, X. Feng, C. Du, S. Wu and W. Song, *J. Mater. Chem. A*, 2015, **3**, 16050–16056.

37 Z. Wang, J. Zhao, Q. Cai and F. Li, *J. Mater. Chem. A*, 2017, **5**, 9842–9851.

38 O. M. Na, N. T. X. Huynh, P. T. Thi, V. Chihaia and D. N. Son, *RSC Adv.*, 2020, **10**, 8460–8469.

39 S. Barja, S. Wickenburg, Z.-F. Liu, Y. Zhang, H. Ryu, M. M. Ugeda, Z. Hussain, Z.-X. Shen, S.-K. Mo, E. Wong, M. B. Salmeron, F. Wang, M. F. Crommie, D. F. Ogletree, J. B. Neaton and A. Weber-Bargioni, *Nat. Phys.*, 2016, **12**, 751–756.

40 W. Jolie, C. Murray, P. S. Weiß, J. Hall, F. Portner, N. Atodiresei, A. V. Krasheninnikov, C. Busse, H.-P. Komsa, A. Rosch and T. Michely, *Phys. Rev. X*, 2019, **9**, 011055.

41 Y. Ma, H. C. Diaz, J. Avila, C. Chen, V. Kalappattil, R. Das, M.-H. Phan, T. Čadež, J. M. P. Carmelo, M. C. Asensio and M. Batzill, *Nat. Commun.*, 2017, **8**, 14231.

42 G. Ye, Y. Gong, J. Lin, B. Li, Y. He, S. T. Pantelides, W. Zhou, R. Vajtai and P. M. Ajayan, *Nano Lett.*, 2016, **16**, 1097–1103.

43 W. Zhan, F. Jia, Y. Yuan, C. Liu, K. Sun, B. Yang and S. Song, *J. Hazard. Mater.*, 2020, **384**, 121382.

44 J. Petö, T. Ollár, P. Vancsó, Z. I. Popov, G. Z. Magda, G. Dobrik, C. Hwang, P. B. Sorokin and L. Tapasztó, *Nat. Chem.*, 2018, **10**, 1246–1251.

45 J. Li, T. Joseph, M. Ghorbani-Asl, S. Kolekar, A. V. Krasheninnikov and M. Batzill, *Nanoscale*, 2021, **13**, 1038–1047.

46 J. P. Perdew, K. Burke and M. Ernzerhof, *Phys. Rev. Lett.*, 1996, **77**, 3865–3868.

47 G. Kresse and J. Furthmüller, *Comp. Mat. Sci.*, 1996, **6**, 15.

48 G. Kresse and J. Furthmüller, *Phys. Rev. B: Condens. Matter Mater. Phys.*, 1996, **54**, 11169–11186.

49 S. Grimme, *J. Comput. Chem.*, 2006, **27**, 1787–1799.

50 A. Tkatchenko and M. Scheffler, *Phys. Rev. Lett.*, 2009, **102**, 073005.

51 Y. Hao, P.-L. Gong, L.-C. Xu, J. Pu, L. Wang and L.-F. Huang, *ACS Appl. Mater. Interfaces*, 2019, **11**, 46327–46336.

52 S. Tian, C. Deng, Y. Tang and Q. Tang, *J. Phys. Chem. C*, 2020, **124**, 24899–24907.

53 A. Kulkarni, S. Siahrostami, A. Patel and J. K. Nørskov, *Chem. Rev.*, 2018, **118**, 2302–2312.

54 M. Chase, *NIST-JANAF Thermochemical Tables*, American Institute of Physics, vol. 1, 1998, 4th edn.

55 C. Ataca and S. Ciraci, *Phys. Rev. B: Condens. Matter Mater. Phys.*, 2012, **85**, 195410.

56 G. Levita, P. Restuccia and M. Righi, *Carbon*, 2016, **107**, 878–884.

57 B. Akdim, R. Pachter and S. Mou, *Nanotechnology*, 2016, **27**, 185701.

58 R. C. Longo, R. Addou, S. KC, J.-Y. Noh, C. M. Smyth, D. Barrera, C. Zhang, J. W. P. Hsu, R. M. Wallace and K. Cho, *2D Materials*, 2017, **4**, 025050.

59 J. Karthikeyan, H.-P. Komsa, M. Batzill and A. V. Krasheninnikov, *Nano Lett.*, 2019, **19**, 4581–4587.

60 H. Shu, D. Zhou, F. Li, D. Cao and X. Chen, *ACS Appl. Mater. Interfaces*, 2017, **9**, 42688–42698.

61 J. K. Nørskov, J. Rossmeisl, A. Logadottir, L. Lindqvist, J. R. Kitchin, T. Bligaard and H. Jónsson, *J. Phys. Chem. B*, 2004, **108**, 17886–17892.

62 Y. Jia, L. Zhang, A. Du, G. Gao, J. Chen, X. Yan, C. L. Brown and X. Yao, *Adv. Mater.*, 2016, **28**, 9532–9538.

63 S. Sinthika, U. V. Waghmare and R. Thapa, *Small*, 2018, **14**, 1703609.